Soft Matter

PAPER

View Article Online
View Journal | View Issue

Cite this: *Soft Matter*, 2014, **10**, 5269

Phase separation and self-assembly of colloidal dimers with tunable attractive strength: from symmetrical square-wells to Janus dumbbells

Gianmarco Munaò,*[a] Patrick O'Toole,[b] Toby S. Hudson,[b] Dino Costa,[a] Carlo Caccamo,[a] Achille Giacometti[c] and Francesco Sciortino[d]

Received 12th March 2014
Accepted 6th May 2014

DOI: 10.1039/c4sm00544a

www.rsc.org/softmatter

We numerically investigate colloidal dimers with asymmetric interaction strengths to study how the interplay between molecular geometry, excluded volume effects and attractive forces determines the overall phase behavior of such systems. Specifically, our model is constituted by two rigidly-connected tangent hard spheres interacting with other particles in the first instance *via* identical square-well attractions. Then, one of the square-well interactions is progressively weakened, until only the corresponding bare hard-core repulsion survives, giving rise to a "Janus dumbbell" model. We investigate structure, thermodynamics and phase behavior of the model by means of successive umbrella sampling and Monte Carlo simulations. In most of the cases, the system behaves as a standard simple fluid, characterized by a gas–liquid phase separation, for sufficiently low temperatures. In these conditions we observe a remarkable linear scaling of the critical temperature as a function of the interaction strength. But, as the interaction potential approaches the Janus dumbbell limit, we observe the spontaneous formation of self-assembled lamellar structures, preempting the gas–liquid phase separation. Comparison with previous studies allows us to pinpoint the role of the interaction range in controlling the onset of ordered structures and the competition between the formation of these structures and gas–liquid condensation.

I Introduction

Recent investigations of the phase behavior of colloidal particles have shown that anisotropies in the molecular geometry, as well as in the properties of interactions, give rise to a variety of different phase equilibria and self-assembled structures.[1,2] With reference to the present study, considerable attention is currently paid to colloidal dumbbells—*i.e.* particles composed by two connected colloidal spheres—especially because of the modern ability to synthesize such molecules with a rich assortment of aspect ratio, size and interaction properties, including dumbbells with asymmetric functionalization of the two component spheres.[3–10] As for the technological impact, recent studies have demonstrated the use of dumbbell colloids as building blocks for the fabrication of new materials,[11] photonic crystals,[12] self-assembled structures under the effect of electric fields[13] and other complex structures.[14]

Theoretical and simulation studies play a significant role in understanding the collective behavior of these colloids. In particular, recent studies of hard dumbbells have focused on their thermodynamic and structural properties,[15–17] the stability of disordered crystal structures,[18] the nucleation processes[19] and the density profiles under confinement.[20] In the case of square-well (SW) dumbbells, it has been shown that the phase behavior sensitively depends on the aspect ratio of the molecule and the strength of attractive interactions;[21–23] these may be tuned to promote the development of spherical clusters (micelles) becoming more and more structured as the temperature is lowered.[24] For strong interaction strengths, as compared to the thermal energy, colloidal dumbbells may also form a gel[25,26] or a glass.[27] All such studies have been carried out in the more general perspective of investigating the self-assembled structures and phase behavior of simple colloidal models to be used as prototypes for a variety of molecular systems whose structural and thermodynamic properties are currently under scrutiny.

In this work we carry out a Monte Carlo simulation study of prototype dumbbell colloids, in order to investigate how the interplay between steric effects, due to the molecular geometry, and the asymmetries in the attractive interactions influences the overall appearance of the fluid phase diagram. Specifically (see Fig. 1), we study a particular class of dumbbell models,

[a]*Dipartimento di Fisica e di Scienze della Terra, Università degli Studi di Messina, Viale F. Stagno d'Alcontres 31, 98166 Messina, Italy. E-mail: gmunao@unime.it as*
[b]*School of Chemistry, University of Sidney, NSW 2006, Australia*
[c]*Dipartimento di Scienze Molecolari e Nanosistemi, Università Ca' Foscari Venezia, Calle Larga S. Marta DD2137, Venezia I-30123, Italy*
[d]*Dipartimento di Fisica, Università di Roma "Sapienza", Piazzale Aldo Moro 2, 00185 Roma, Italy*

initially formed by two identical tangent hard spheres, each surrounded by an attractive square-well with an interaction range fixed at half the hard-core diameter. Then, one of the SW interaction is weakened—by progressively reducing the corresponding well depth till nought—so to end up with only a bare hard-sphere repulsion left on one site. We document how the features of microscopic interactions sensitively determine a competition between gas–liquid phase separation and the spontaneous formation of different self-assembled structure in the fluid.

We compare our results with other recent studies, in which some of the authors have been involved,[24,28] so to determine more extensively the role played by both the interaction properties and the model geometry. In particular, ref. 24 has been partly devoted to the study of a similar class of SW dumbbells, in which the attraction range is only one-tenth of the hard-core diameter. We shall show how the enlargement of the attraction range modifies the stability, position and shape of the gas–liquid coexistence curves, and, correspondingly, we document different trends in the behavior of critical parameters. Moreover, the SW range plays a prominent role in the spontaneous development of peculiar planar structures (lamellæ), apparently observed only for larger attractions. The development of lamellar aggregates has been observed in a large variety of model systems, including charged colloids,[29–31] asymmetric amphiphatic particles,[32] soft asymmetric dumbbells[33] and Janus particles;[34,35] as we shall see, the properties of lamellar aggregates developing in our system closely correspond to those observed in fluid composed by one-patch colloids,[28] *i.e.* spherical particles in which the attractive interaction is reduced to a sticky patch on the surface.

The model constituted by a bare hard-sphere interaction on one site plus a SW interaction on the other one site (see right panel of Fig. 1), may be considered as a "Janus dumbbell",[36,37] constituting a molecular generalization of the well-known concept of Janus spherical particle,[38–46] in which one-half of the surface is attractive and the other one-half is repulsive. Previous investigations carried out by some of the authors[47,48] on Janus particles interacting *via* SW with the same attractive range of the present model, have shown that the fluid is characterized by an anomalous phase behavior, with the gas–liquid coexistence curve negatively sloped in the temperature–pressure plane. Here we compare such a picture with what we observe for Janus dumbbells, for which we anticipate that the gas–liquid phase separation is preempted by the formation of lamellar aggregates in the fluid.

As for Monte Carlo simulations, we have employed the Successive Umbrella Sampling (SUS) technique,[49] complemented by histogram reweighting,[50] to calculate the gas–liquid coexistence points. In addition, we have carried out simulations at constant temperature and pressure (NPT) to investigate the thermodynamic and structural properties for the peculiar dumbbell model in which one of the interaction strengths is set equal to one tenth of the other one.

The paper is organized as follows: in Section II we detail the interaction properties of our dumbbell models and the simulation techniques we have employed in this study. Results are reported and discussed in Section III. Conclusions follow in Section IV.

II Models and methods

The sequence of models investigated in this work is sketched in Fig. 1. The starting point (SW dumbbell, left panel) is constituted by two tangent hard spheres of diameter σ (labeled as sites 1 and 2 in the figure), interacting with sites 1 and 2 of another dumbbell at distance r *via* identical square-well attractions, specifically

$$V_{11}(r) \equiv V_{12}(r) \equiv V_{22}(r) = V_{HS}(r) + V_{SW}(r) \quad (1)$$

where

$$V_{HS}(r) = \begin{cases} \infty & \text{if} \quad r < \sigma \\ 0 & \text{otherwise} \end{cases} \quad (2)$$

and

$$V_{SW}(r) = \begin{cases} -\varepsilon & \text{if} \quad \sigma \le r < \sigma + \lambda\sigma \\ 0 & \text{otherwise} \end{cases} \quad (3)$$

Parameters σ and ε entering eqn (2) and (3) provide, respectively, the unit of length and energy, in which terms we define the reduced temperature $T^* = k_B T/\varepsilon$ (with k_B as the Boltzmann constant), density $\rho^* = (N/V)\sigma^3$ (where N is the number of particles and V the volume) and pressure $P^* = P\sigma^3/\varepsilon$.

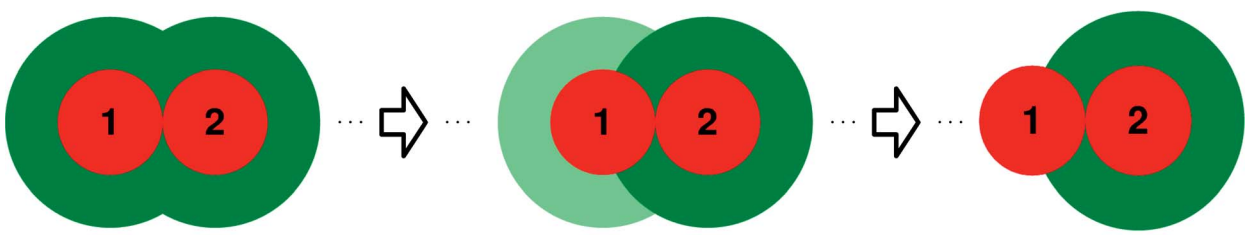

Fig. 1 Models investigated in this work. Symmetrical square-wells (left panel, where the inner circles represent the hard spheres and the outer coronas the square-well interactions) and Janus dumbbells (right panel, where one of the square-well interaction is completely switched off) are connected by a series of intermediate models with "fading" square-well strength (at fixed range $\lambda = 0.5$) on one of the two interaction sites (middle panel).

In all calculations we have fixed $\lambda = 0.5$. At the opposite end (Janus dumbbell, right panel of Fig. 1), the SW attraction on site 1 is completely switched off, so that the mutual interactions among sites on different molecules become:

$$V_{11}(r) \equiv V_{12}(r) = V_{HS}(r)$$
$$V_{22}(r) = V_{HS}(r) + V_{SW}(r). \quad (4)$$

In order to understand the properties of our systems on moving between these two models, we have studied a sequence of intermediate cases (central panel of Fig. 1) obtained by progressively reducing the square-well depth of site 1 from $\varepsilon_1 = 1$ (in unit of ε) to $\varepsilon_1 = 0$, corresponding, respectively, to the SW and Janus dumbbell models. Such intermediate models are again described by eqn (1)–(3), but for the replacement of ε with ε_1 in the $V_{11}(r)$ and $V_{12}(r)$ interactions. In particular, we have investigated the cases $\varepsilon_1 = 1$, 0.70, 0.50, 0.30, 0.20, 0.15, 0.10, 0.05, 0.025, 0.

To determine the gas–liquid coexistence conditions, we have calculated for each model the coexisting densities at several different temperatures by means of SUS simulations[49] in the grand canonical ensemble. According to this technique, the number of particles in the system, ranging from zero to N_{max}, is divided into many small windows of size ΔN. For each window i in the interval $N \in [N_i, N_i + \Delta N]$, we have carried out a grand-canonical MC simulation, avoiding the insertion or deletion of particles outside the range of the window.[51] This procedure allows one to calculate the histogram H_i monitoring how often a state with N particles is visited in window i. The full probability of densities is then given by the following product:

$$\frac{P(N)}{P(0)} = \frac{H_0(1)}{H_0(0)} \times \frac{H_0(2)}{H_0(1)} \cdots \times \frac{H_0(\Delta N)}{H_0(\Delta N - 1)} \cdots \times \frac{H_i(N)}{H_i(N-1)} \quad (5)$$

The advantage of using such a method relies both in the possibility to sample all microstates without any biasing function and in the relative simplicity to parallelize the run, with the speed gain scaling linearly with the number of processors. Once $P(N)$ is obtained at fixed temperature, we have applied the histogram reweighting technique,[50] that emulates the effect of adjusting the chemical potential, to eventually obtain the coexistence points. This is done by reweighting the densities histogram until the regions below the two peaks (in the low- and high-density phases) attain the same area. Finally, we have fitted the calculated gas–liquid coexistence points by means of the scaling law for the densities and the law of rectilinear diameters, with an effective non-classical exponent $\beta = 0.32$,[52] in order to determine the full gas–liquid coexistence curves together with the corresponding critical points.

The peculiar case $\varepsilon_1 = 0.1$ has been investigated also by NPT Monte Carlo simulations. We have employed to this purpose 343 molecules enclosed in a cubic box with standard periodic boundary conditions. For each state point, twenty million Monte Carlo sweeps, each consisting of one trial move per particle, have been equally divided in order to first equilibrate the system and then to collect data.

III Results and discussion

Selected density distribution probabilities $P(\rho)$, as obtained by SUS simulations, are reported in Fig. 2a for several values of ε_1. Specifically, such probabilities correspond to the temperatures whereby $P(\rho)$ first displays a double-peak behavior, providing indication on the position of critical points. In all simulations we have employed a box length $L_{box} = 13.57\sigma$ but for $\varepsilon_1 = 0.1$, for which $L_{box} = 20\sigma$. The gas–liquid coexistence curves are reported in panel (b) of the same figure.

Critical temperatures, T_c^*, and densities, ρ_c^*, as functions of ε_1, are shown in Fig. 3. Numerical values are reported in Table 1. As visible, the critical temperature decreases almost linearly with ε_1; on the other hand, the critical density stays almost constant ($\rho_c^* \approx 0.15$) for high values of the interaction strength, with a drastic decrease for lower values, as signaled by the "knee" at

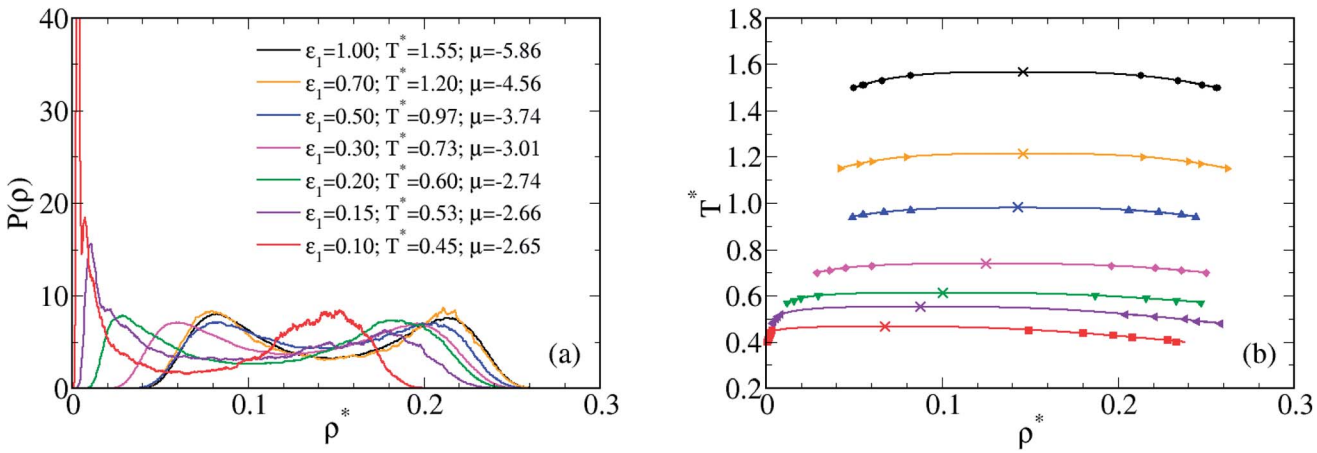

Fig. 2 Panel (a): SUS density distribution probabilities $P(\rho)$ for different ε_1; data are reported at reduced temperatures and chemical potentials (in unit of ε) whereby $P(\rho)$ first displays a double-peak behavior. Panel (b): SUS gas–liquid coexistence points (symbols) for different ε_1, with corresponding critical points (crosses). Lines are the interpolations of simulation points obtained by the scaling law for the densities and the law of rectilinear diameters;[52] color convention for ε_1 as in panel (a).

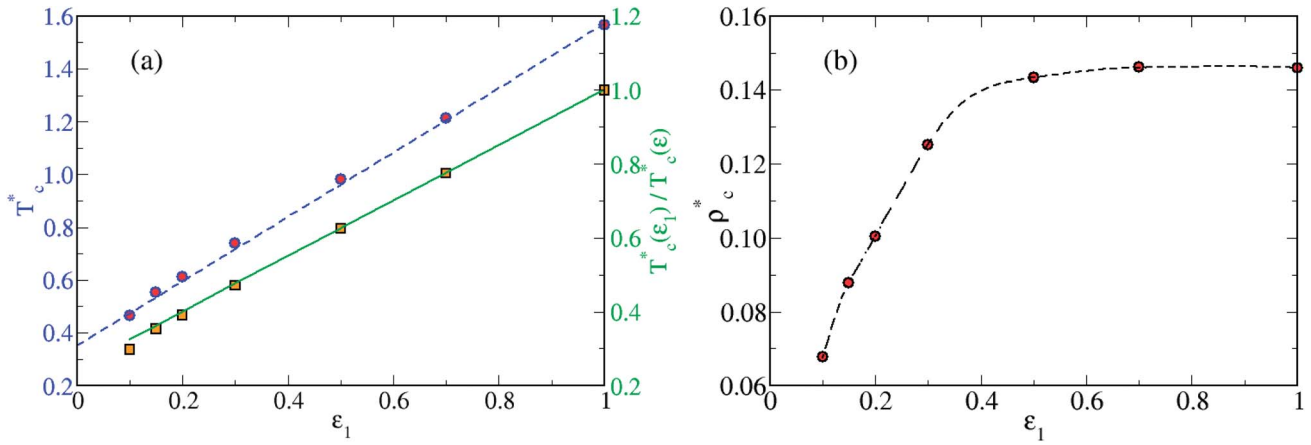

Fig. 3 Critical temperatures (panel (a), circles, scale on the left, blue) and densities (panel (b)) as functions of ε_1; dashed lines are guides to the eye. In panel (a) we also show the comparison between results obtained from simulations (squares) and mean-field scaling (full line) for $T^*_c(\varepsilon_1)/T^*_c(\varepsilon)$ (scale on the right, green).

Table 1 Critical parameters of different models investigated in this work. Uncertainties correspond to the accuracy with which we have ascertained the first occurrence of a double peak in $P(\rho)$

ε_1	T^*_c	ρ^*_c
1.00	1.56 ± 0.01	0.146 ± 0.001
0.70	1.21 ± 0.01	0.146 ± 0.002
0.50	0.98 ± 0.01	0.143 ± 0.002
0.30	0.74 ± 0.01	0.125 ± 0.004
0.20	0.61 ± 0.01	0.10 ± 0.01
0.15	0.55 ± 0.02	0.09 ± 0.01
0.10	0.47 ± 0.02	0.07 ± 0.02

$\varepsilon_1 \approx 0.5$. Fig. 2b documents how the observed decrease of ρ^*_c for $\varepsilon_1 < 0.5$ is due to a progressive shift of the gas branch of the coexistence curve towards lower densities. Such a trend is not accompanied by a corresponding shift in the liquid branch; as a consequence, the binodal curve appears "stretched", loosing the rather symmetrical shape observed for $\varepsilon_1 \geq 0.5$.

The observed linear trend of T^*_c is suggestive of a mean-field behavior that can be rationalized as follows. The interaction between two dumbbells labeled a and b can be alternatively described by an anisotropic potential $V_{ab} = V(\mathbf{r}_{ab}, \hat{\mathbf{u}}_a, \hat{\mathbf{u}}_b)$, where $\mathbf{r}_{ab} = \mathbf{r}_b - \mathbf{r}_a$, and where $\hat{\mathbf{u}}_a$ and $\hat{\mathbf{u}}_b$ are unit vectors indicating the dumbbells orientation in space, as directed from the 1 to the 2 spheres, associated with solid angles ω_a and ω_b respectively. Upon introducing the angular average $\langle \ldots \rangle_\omega = (1/4\pi)\int d\omega \ldots$, the exact second virial coefficient, reading

$$B_2(T^*) = -\frac{1}{2}\int d\mathbf{r}_{ab}\left\langle \exp\left[-\frac{V_{ab}}{T^*}\right] - 1\right\rangle_{\omega_a,\omega_b}, \quad (6)$$

becomes, within a mean-field approximation,

$$B_2^{MF}(T^*) = -\frac{1}{2}\int d\mathbf{r}_{ab}\exp\left[-\frac{\langle V_{ab}\rangle_{\omega_a,\omega_b}}{T^*}\right] - 1. \quad (7)$$

Finally, within the interaction-site approach, we can make the replacement

$$\langle V_{ab}\rangle_{\omega_a,\omega_b} = \frac{1}{4}\sum_{i\neq j} V_{ij}(r_{ab}) = V^{MF}(r_{ab}) \quad (8)$$

where $r_{ab} = |\mathbf{r}_{ab}|$, and $V^{MF}(r_{ab})$ is a square-well potential akin to eqn (3) but associated with a mean-field energy given by $\varepsilon_{MF} = (3\varepsilon_1 + \varepsilon)/4$ (note that out of the four site–site interactions, one is a square well with energy ε and three have energy ε_1). As for fixed λ the critical temperature only depends upon the energy scale, this leads to the relation

$$\frac{T^*_c(\varepsilon_1)}{T^*_c(\varepsilon)} = \frac{3\varepsilon_1 + \varepsilon}{4\varepsilon} = \frac{1}{4}\left(1 + 3\frac{\varepsilon_1}{\varepsilon}\right). \quad (9)$$

The accuracy of a mean-field hypothesis is documented in Fig. 3a, where we show how eqn (9) positively reproduces SUS data, but for the small discrepancy visible around $\varepsilon_1 = 0.1$. On the other hand, the observed behavior of ρ^*_c *vs.* ε_1 prevents the possibility to extend such a mean-field treatment also to the critical density. Our previous study[24] concerned a similar sequence of square-well dumbbells with an attractive range $\lambda = 0.1$, shorter than that employed here (*i.e.* $\lambda = 0.5$). A comparison shows that in both cases the critical temperatures scale almost linearly with ε_1, apart from the expected shift toward lower values observed for $\lambda = 0.1$, due to the shorter range of interactions. On the other hand, the critical density for $\lambda = 0.1$ keeps an almost constant value ($\rho^*_c \simeq 0.21$), at variance with the drastic changes reported in Fig. 3b.

Overall, on a relatively large interval of ε_1 values ($\varepsilon_1 > 0.1$) the system behaves as a standard "simple fluid", with a supercritical state at high temperatures making way to a gas–liquid phase separation as the temperature is lowered. This scenario is exemplified in Fig. 4a, referring to $\varepsilon_1 = 0.5$.

Around $\varepsilon_1 \approx 0.1$ a different scenario arises. A focus on the properties of the system regarding the case $\varepsilon_1 = 0.1$ is given in Fig. 5 where, in panel (a), we display the SUS probability

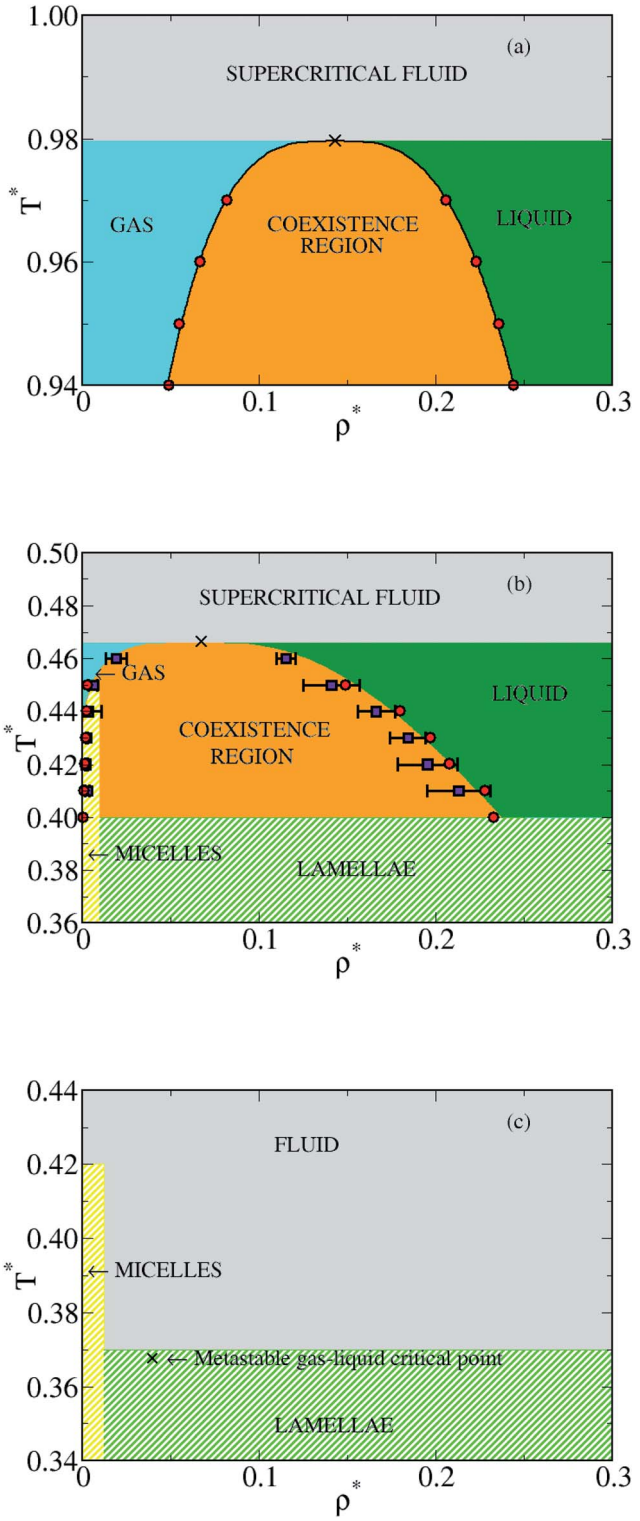

Fig. 4 Progressive schematic modification of the fluid phase diagram as estimated by SUS simulations upon lowering ε_1 from (a) 0.5 to (b) 0.1 till (c) 0.025. Circles are gas–liquid coexistence points whereas crosses mark the relative critical points. Squares in panel (b) are coexistence points estimated by NPT simulations.

distribution of the number of particles $P(N)$ at $T^* = 0.45$ and two different simulation box sizes. The two main peaks visible in the figure testify the existence of stable gas and liquid phases, with corresponding critical point at $T_c^* \approx 0.47$ (see Table 1). We notice that the position of the gas peak in $P(N)$ is shifted toward extremely low values of N, indicating a rather low gas density.

Beside the gas and liquid peaks, $P(N)$ in Fig. 5a is now characterized by the appearance of a third peak (see also the magnification in the inset) that does not scale with the box size. Such new feature signals the presence of aggregates (micelles) in the low density regime of the fluid. The analysis of microscopic configurations shows that micelles grow in the form of roughly spherical clusters formed by a variable number of particles typically ranging within few tenths (see Fig. 5b). We have ascertained the presence of such spontaneously formed aggregates over a temperature range extending down to the lowest temperature investigated for this case ($T^* = 0.36$), albeit confined on a narrow (low) density interval. When aggregation takes place, finite size effects become relevant and the SUS data must be carefully scrutinized: specifically, we have ascertained that the micelles peak does not point to the presence of a true thermodynamic phase as it invariably falls at the same number of particles independently on the simulation box size. In other words, as documented in Fig. 5a, when a larger simulation box is employed, the positions of peaks corresponding to the gas and liquid phases in the $P(N)$ *vs.* N diagram turn to be shifted (so to keep constant the corresponding coexisting densities), whereas the micelles peak is left unchanged. Conversely, within a $P(\rho)$ *vs.* ρ representation, the gas and liquid peaks maintain the same positions, whereas the micelles peak shift toward lower densities.[53] The formation of micelles takes places at low temperatures and low densities. At low temperatures ($T^* \approx 0.40$) and larger densities, visual inspection of microscopic configuration reveals that molecules self-assemble into a different form, represented by planar structures (lamellæ), and extending till the highest density value investigated in this study, *i.e.* $\rho^* = 0.3$. A representative snapshot of such spontaneously formed structures is given in Fig. 5c, while in panel (d) of the same figure we report the bond probability distribution $P(N_b)$ of different aggregation forms observed in the fluid, with N_b defined as the number of bonds per particle. Here two particles are considered as bonded together if any of their site–site distances falls within the SW attraction range, *i.e.* between σ and $\sigma + \lambda\sigma$, see eqn (3). As visible, the formation of lamellæ is characterized by a broad peak centered around $N_b = 9$, *i.e.* in such a planar arrangement each dumbbell is preferentially bonded to nine neighbors. Interestingly enough, exactly the same structure has been found recently in ref. 28 in the study of aggregate formation in fluid composed by one-patch colloids. As for the formation of micelles, this is instead characterized by a wider variety of different arrangements, as testified for instance by the presence of multiple peaks in the corresponding bond distribution.

The phase diagram at $\varepsilon_1 = 0.1$ is summarized in Fig. 4b. The peculiar features emerging for such a value of the interaction strength call for a more detailed analysis of structural and thermodynamic properties of the system, that we have carried

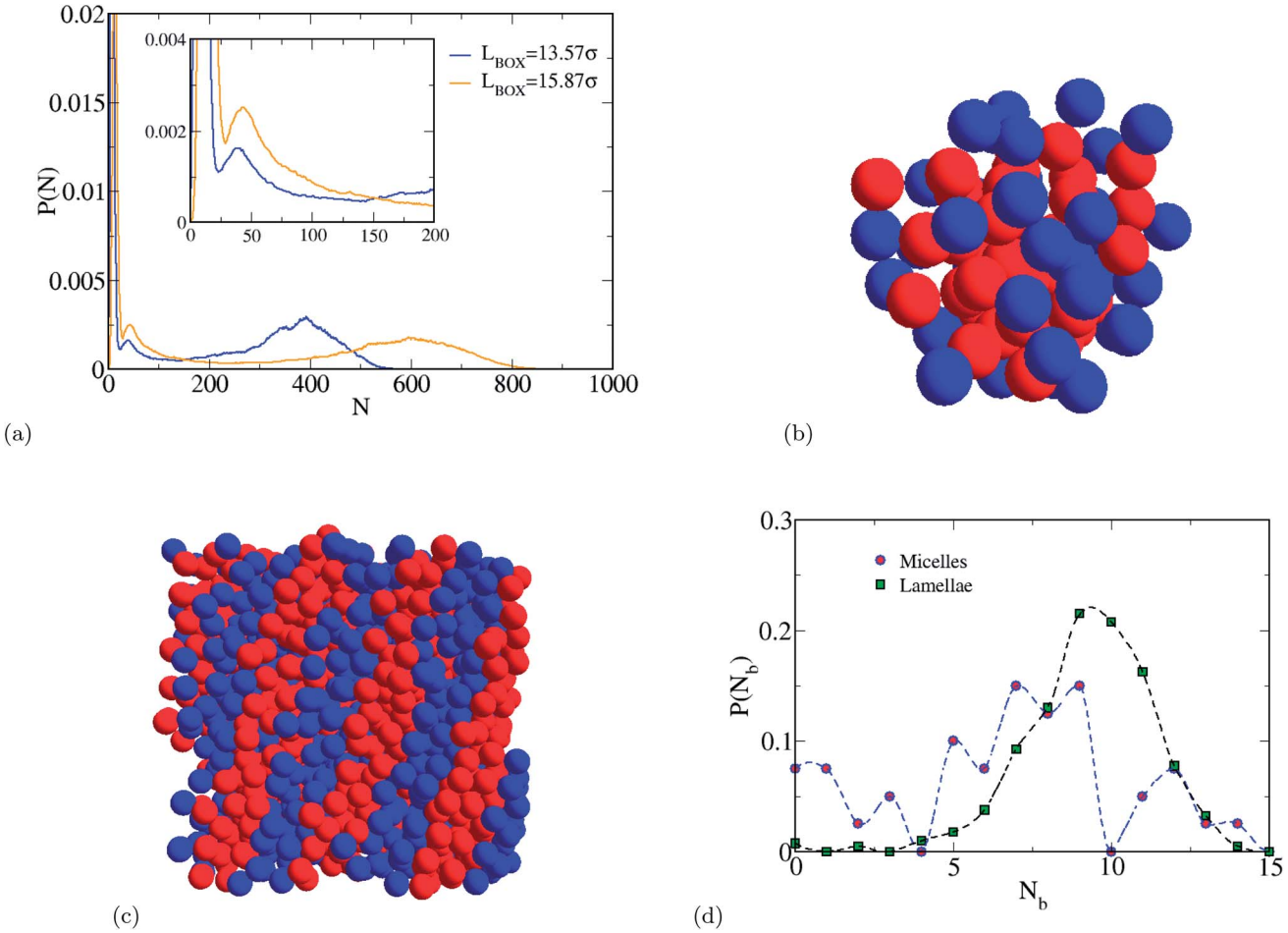

Fig. 5 Focus on the case $\varepsilon_1 = 0.1$. Panel (a): probability distribution of the number of particles $P(N)$ at $T^* = 0.45$ and two different box sizes with a magnification of micellar peaks in the inset. Typical microscopic configurations of self-assembled structures developed in the system, *i.e.* micelles (panel (b)) and lamellæ (panel (c)), observed at $T^* = 0.38$. Panel (d): bond probability distributions $P(N_b)$ for different aggregates at $T^* = 0.38$.

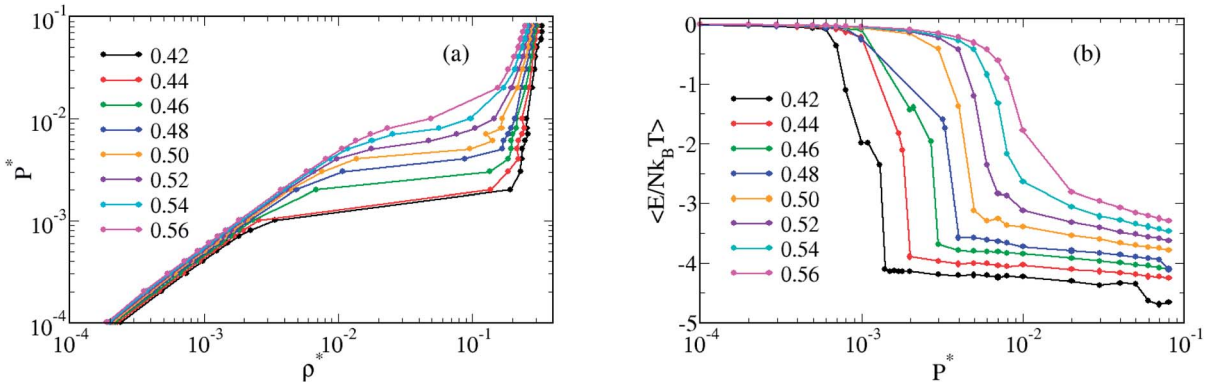

Fig. 6 Equation of state (a) and energy *vs.* pressure (b) at $\varepsilon_1 = 0.1$ and different temperatures, indicated in the legends.

out by means of NPT Monte Carlo simulations. In Fig. 6 we report, for several temperatures, the equation of state in the pressure–density plane, and the internal energy as a function of the pressure. For $0.41 \leq T^* \leq 0.48$, sub-critical phenomena can be resolved, showing a discontinuity in the density, while for $T^* \geq 0.48$ a continuous transition is observed. The corresponding density discontinuity appears to reduce in magnitude upon increasing the temperature, until just below the estimated critical temperature $T_c^* \approx 0.47$. The energy per particle in Fig. 6b, observed for pressures where the density deviates markedly from

ideality (for $T^* = 0.42$), but below the density transition, indicates the onset of a particle association process. The onset of a lamellar phase for $P^* > 0.06$ at $T^* < 0.41$ is seen here by a marginally lower energy per particle. In spite of having a comparatively low energy and the clustering process taking shape here, we have observed no anomalous behavior akin to that of Janus colloids, where for instance the gas–liquid coexistence curve turns to be negatively sloped in the temperature–pressure plane.[47,54] The condensation process occurs without hindrance from comparatively stable clusters, due to the fact that these latter do not take on well defined "hard" surface morphologies, *i.e.* with the strongly interacting spheres facing inward. This contrasts with the Janus sphere case, where the angular dependence of a favorable interaction promotes the orientation of the "hard" interaction outward, effectively rendering each cluster–cluster interaction rigid enough to prevent cluster merging processes, until the system is dense enough.

In Fig. 4b we report, beside the SUS data, also the phase coexistence points as obtained by Maxwell construction on the equation of state in Fig. 6a. Specifically, we have calculated the slope of the ultimate three points from either side of the transition at the corresponding temperatures and projected straight lines to a point where the pressure is equal. Error bars correspond to the average distance between density at the projected coexistence pressure and last Monte Carlo data point with the projected point corresponding to the pressure of the final data point of the other side of the transition. As visible, NPT estimates satisfactorily agree with SUS calculations.

Typical liquid site–site radial distribution functions $g(r)$, showing the preferential interaction of sites 2–2 and 1–1 are reported in Fig. 7. The 2–2 peak shows a preference for the bond lengths to occupy the inner-most and outer-most extents of the interaction range λ. The comparatively lower curve representing the 1–1 interaction can be attributed to the relative larger binding energy of the 2–2 interaction. The second, almost discontinuous peak of the 1–1 curve around $r = 2\sigma$ would seemingly imply a preference for a significant proportion of the particles to be with sites 1 at 180 degrees to each other, as depicted in the snapshot of Fig. 5c.

In Fig. 8 we report the orientational order parameter $P(u_1 \cdot u_2)$, defined as:

$$P(u_1 \cdot u_2) \equiv \langle \cos(\theta_{12}) \rangle \quad (10)$$

where θ_{12} is the angle between a unit vector pointing from the site 2 to the site 1 of different dumbbells. Data in the figure concern $P(u_1 \cdot u_2)$ as calculated at $T^* = 0.40$ and increasing pressure; a normalization factor has been employed to make the total integral under the curves unity, with 1024 bins for the distribution. As visible, between $P^* = 0.06$ and 0.08 the system has already started to display lamellar character. Increasing the pressure causes the lamellar structure to become more defined and the order parameter to appear increasingly quartic. As for the development of micelles, we have not observed a global alignment in the unit vectors. The reason for this is twofold: firstly, there is no correlation between the orientation of particles in different clusters as they do not communicate through a planarity imposed by adjacent lamellar structures; secondly, as the interaction potential does not have an angular component, the favorable energetic configuration between any two particles can be maintained without the requirement of a certain

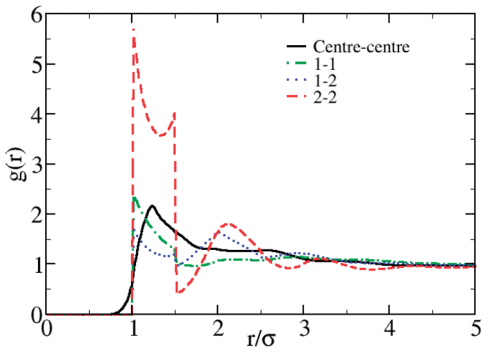

Fig. 7 Centre–centre and site–site radial distribution functions $g(r)$ for $\varepsilon_1 = 0.1$ at $P^* = 0.0011$ and $T^* = 0.43$.

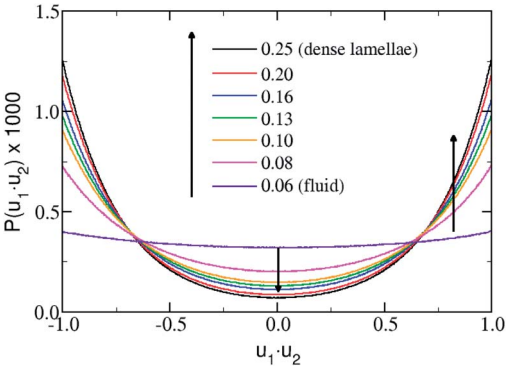

Fig. 8 Orientational order parameter $P(u_1 \cdot u_2)$ for $T^* = 0.40$ and increasing pressures. The onset of the lamellar phase is seen here as a peak resolving in the $|\cos(\theta)| \rightarrow 1$.

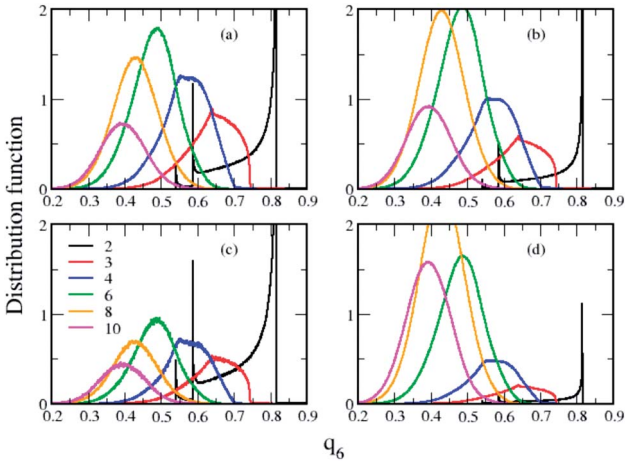

Fig. 9 Distributions of q_6 for several values of N_b (color convention in the legend of panel (c)). Top panels refer to $T^* = 0.46$ with $\rho^* \approx 0.009$ (a) and $\rho^* \approx 0.120$ (b); bottom panels, $T^* = 0.42$ with $\rho^* \approx 0.001$ (c) and $\rho^* \approx 0.220$ (d).

alignment; rather the two bonded particles have only a very small restricted space of mutual orientations (their comparatively hard components cannot themselves overlap). We expect that the study of the radial dependence of $P(u_1 \cdot u_2)$—not carried out here—should allow the observation of some structure, as particles with distance $r \approx \langle D_m \rangle$ (where $\langle D_m \rangle$ is the average diameter of a micelle), will tend to have an opposing orientation leading to a strong peak around $\langle D_m \rangle$, and likely a weaker peak at $r \approx \langle r_c \rangle$, with $\langle r_c \rangle$ the average distance between clusters.

In Fig. 9 we report the rotational invariant of local bond order parameters q_6 (see ref. 55 and references therein), to probe the dependence of bond orientations on the interaction potential, in both micelles and the liquid phase. We have considered only bonds of the 2–2 interactions in the calculation of this metric. Distributions in the figure show well defined structures for particles which make relatively few bonds. The three peaks in the $N_b = 2$ distribution at 0.8135, 0.583 and 0.538 (most clear in the gas phase distributions) correspond to different bonding environments. In the first case the angle between bonds (made by particle i to each of its two neighbors j and j') corresponds to $\pi/3$ radians, *i.e.* an equilateral triangle with $r_{ij} = r_{ij'} = r_{jj'}$ is formed; the second case, $\approx$0.6797 radians, corresponds to an isosceles triangle with $r_{ij} = r_{ij'} = \sigma + \lambda\sigma$ and $r_{jj'} = \sigma$; the third case, $\approx$1.6961 radians, corresponds to $r_{ij} = r_{ij'} = \sigma$ and $r_{jj'} = \lambda\sigma$. The end of the distribution indicates particles whose neighbors number three corresponds to an equilateral triangle based pyramid whose tip, mutually at the furthest extent of the interaction range, is the particle i. Where the number of bonds is greater than four, the ability to easily detect a potential dependence ceases, and no more fine detail is obtainable directly from the distributions of q_6, except for the distribution of numbers of bonds per particle.

Upon approaching the Janus dumbbell case, *i.e.* as $\varepsilon_1 \to 0$, a third different phase scenario arises, as exemplified in Fig. 4c for the case $\varepsilon_1 = 0.025$. As visible, at relatively high temperatures ($T^* \geq 0.42$), the system stays in a homogeneous fluid phase. Lowering the temperature leads to the formation of micelles at low densities, while at intermediate and (relatively) high densities the system is still in a fluid phase. As the temperature is further decreased, below $T^* = 0.38$, the formation of bilayer sheets (lamellæ) is observed as well. The progressive organization of clusters as the number of particles increases is schematically represented in Fig. 10 where we show several different microscopic snapshots of the system with $\varepsilon_1 = 0$ (*i.e.* exactly in the Janus dumbbell limit) at fixed $T^* = 0.31$ and on varying N in a simulation box with a fixed edge of 20σ. As visible, lamellar

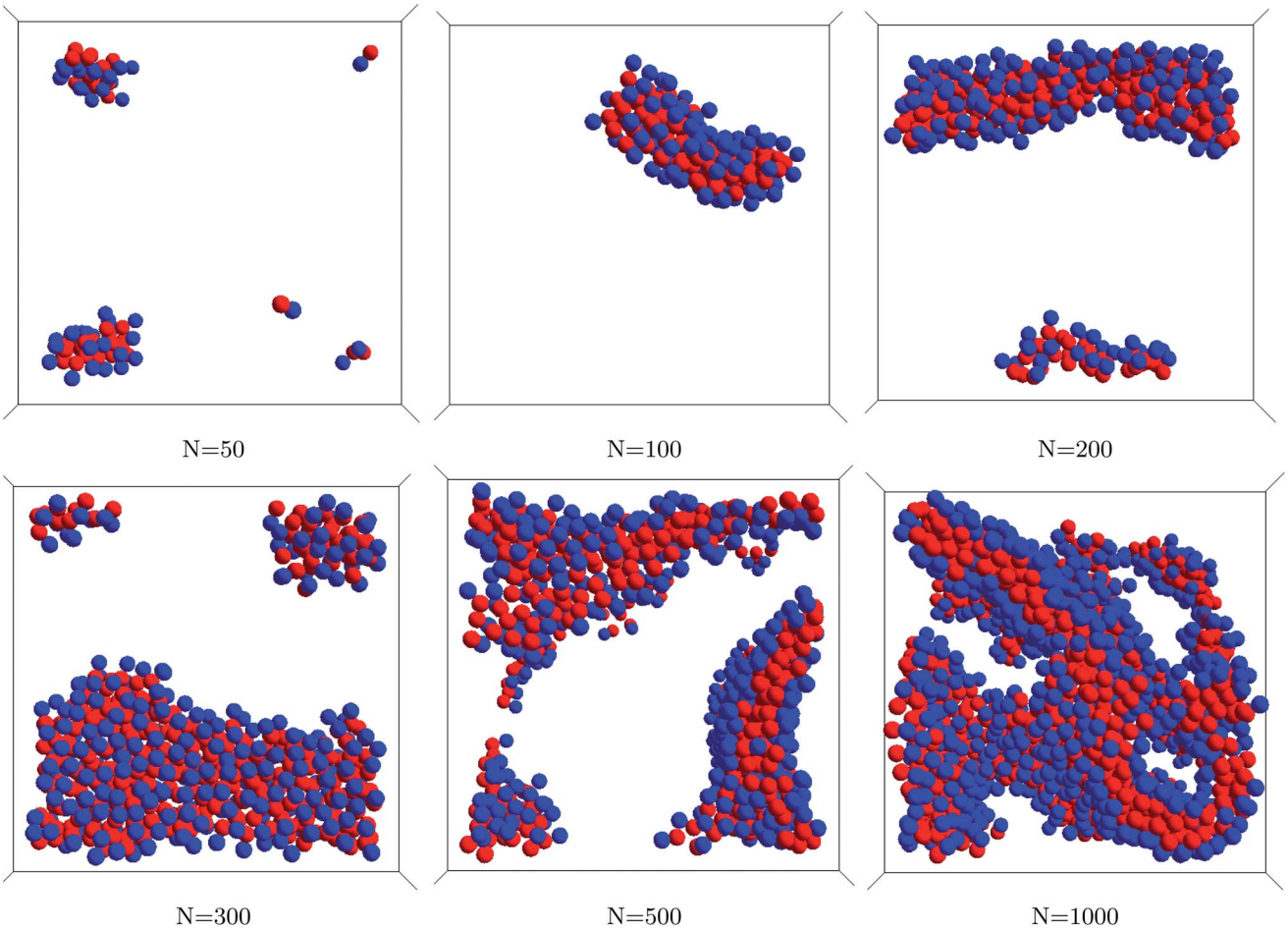

Fig. 10 Snapshots of microscopic configurations concerning the Janus dumbbell model ($\varepsilon_1 = 0$) at $T^* = 0.31$ and increasing number of particles N.

structures appear even at $N = 100$, corresponding to set $\rho^* = 0.0125$. Therefore, the molecular geometry of the model promotes planar configurations rather than spherical aggregates (like micelles), that are observed only at extremely low densities. The onset of aggregation in Janus dumbbells is signalled at the structural level by the behavior of partial structure factors $S(k)$. In Fig. 11 we report in particular the $S_{22}(k)$ at fixed $\rho^* = 0.20$ and decreasing temperatures: the progressive enhancement of a low-k peak (beside the main scattering peak centered around $2\pi/\sigma$), and the simultaneous absence of any diverging trend in the $k \to 0$ limit, provide a picture of a self-assembling fluid (see *e.g.* ref. 24 and 56–58 and references therein), where aggregates become more structured as the temperature is lowered.

The extrapolation of the critical temperature, reported in Fig. 3, leads to the prediction of a hypothetical critical point $T_c^* \approx 0.37$ for $\varepsilon_1 = 0.025$, and slightly lower for Janus dumbbells. However, as shown in the phase diagram of Fig. 4c, the formation of lamellar aggregates preempts the gas–liquid phase separation, implying the metastability (and possibly the absence) of a corresponding critical point. By comparing again with ref. 24, we record the absence of a gas–liquid phase separation in the low ε_1 range both for $\lambda = 0.1$ and for $\lambda = 0.5$. In the former case, however, no evidence for the formation of lamellæ has been detected, and we have attributed the absence of a gas–liquid coexistence to the competition with the formation of cluster aggregates, together with the short-range character of the attractive interaction, bringing the critical point (if any) to a temperature range too low to be numerically investigated. Interestingly enough, a relative large, fivefold increase of the interaction range (from $\lambda = 0.1$ to $\lambda = 0.5$) produces a relative modest enlargement toward lower values of the range of interaction strength for which a stable gas–liquid phase separation can be found (from $\varepsilon_1 \approx 0.2$ to $\varepsilon_1 \approx 0.1$). On the other hand, in the specific case of Janus dumbbells, if we increase the interaction range to the limit $\lambda = 1$, the hard-sphere on the first site would be completely enveloped by the square-well interaction on the second site (see right panel of Fig. 1), becoming much less effective. In this case the behavior of our model would tend to that of a simple square-well monoatomic fluid, having a normal gas–liquid phase separation. In this context, it is interesting to study how "marginal" the presence of the hard-sphere protrusion on one site of our model must be, in order to let a stable gas–liquid coexistence emerge for ε_1 values down to zero, *i.e.* even in the Janus dumbbell case. Meanwhile we observe that, should such a gas–liquid coexistence be observed in the range $\lambda = 0.5$–1, a closer correspondence would be established with the phase behavior of Janus spherical colloids for which, as we mentioned in the Introduction, a stable coexistence between a micellar-gas and a liquid phase is already found for λ values around 0.5.[47] In this latter case, only by decreasing λ to 0.2, the gas–liquid phase separation becomes metastable and new self-assembled structures, like wrinkled sheets, develop in the system.[35,47]

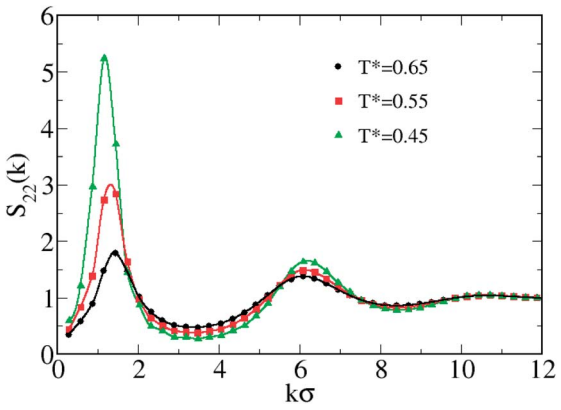

Fig. 11 Enhancement of the low-k peak of $S_{22}(k)$ for Janus dumbbells upon lowering the temperature at fixed $\rho^* = 0.20$.

IV Conclusions

We have studied the gas–liquid phase coexistence and the self-assembly processes taking place in a colloidal model constituted by two tangent dumbbells with square-well interactions, upon varying the attraction strength on one of the two molecular sites. Specifically (see Fig. 1), the two limiting cases are constituted by symmetrical square-wells on the one side, and Janus dumbbells on the other one side, with several cases in between, as obtained by progressively reducing the attraction strength ε_1 of one of the two square-wells. We have employed successive umbrella sampling Monte Carlo simulations to trace the gas–liquid coexistence curves, complemented by NPT Monte Carlo simulations only for the special case $\varepsilon_1 = 0.1$.

We have documented how the unbalance between the square-well attraction strengths, combined with anisotropic steric interactions, gives rise to a rich fluid phase scenario exemplified in Fig. 4. For a wide range of ε_1 values (>0.1) the system behaves as a "simple fluid" showing a normal gas–liquid phase separation below a certain critical temperature. The observed linear scaling of such a temperature with ε_1 can be understood in terms of a simple mean-field argument. As $\varepsilon_1 \to 0.1$, self-assembled structures start to develop, causing a drastic reduction in the temperature–density extension of the gas and liquid coexisting phases. At low densities and temperatures, such structures are constituted by small spherical aggregates (micelles), involving few tenth of particles. At low temperatures and higher densities, we have observed the onset of a different self-assembled structure, in which molecules are organized into planar configurations (lamellæ). As ε_1 is further decreased below 0.1, we have observed no stable gas–liquid phase separation, with the system forming only micelles at low densities and lamellæ at intermediate/high densities. In the case of Janus dumbbells (*i.e.* with $\varepsilon_1 = 0$) lamellar structures take place also at reduced densities as low as 0.0125, suggesting that the specific geometry of tangent Janus dumbbells definitely promotes the development of planar configurations rather than spherical aggregates.

To summarize, the models investigated in this work are useful prototypes to study the role of attractive interactions in tuning cluster formation and/or phase separation in colloidal dimers. The rich phase behavior, together with the relatively

simple design, make our models suitable candidates for a better understanding of the self-assembly processes. In particular, this study has highlighted the difference with the phase diagram of Janus colloids, as well as the interplay between steric effects and interaction anisotropies. Varying the geometric properties of our models (as for instance the ratio between the hard-core diameters[59] or their distance) is expected to add further significant features on the overall phase diagram documented in this work, with a potentially rich scenario.

Acknowledgements

G.M., D.C., C.C., A.G. and F.S. gratefully acknowledge support from PRIN-MIUR 2010–2011 project. G.M. and F.S. acknowledge support from ERC-226207-PATCHYCOLLOIDS. Also, A.G., P.O'T. and T.S.H. acknowledge the support of a Cooperlink bilateral agreement Italy–Australia.

References

1 A. Yethiraj and A. van Blaaderen, *Nature*, 2003, **421**, 513.
2 Y. Wang, Y. Wang, D. R. Breed, V. N. Manoharan, L. Feng, A. D. Hollingsworth, M. Weck and D. Pine, *Nature*, 2012, **491**, 51.
3 J.-W. Kim, R. J. Larsen and D. A. Weitz, *J. Am. Chem. Soc.*, 2006, **128**, 14374.
4 E. Lee, Y.-H. Jeong, J.-K. Kim and M. Lee, *Macromolecules*, 2007, **40**, 8355.
5 M. Hoffmann, Y. Lu, M. Schrinner, M. Ballauff and L. Harnau, *J. Phys. Chem. B*, 2008, **112**, 14843.
6 M. Hoffmann, C. S. Wagner, L. Harnau and A. Witteman, *ACS Nano*, 2009, **3**, 3326.
7 M. Hoffmann, M. Siebenburger, L. Harnau, M. Hund, C. Hanske, Y. Lu, C. S. Wagner, M. Drechsler and M. Ballauff, *Soft Matter*, 2010, **6**, 1125.
8 S. Chakrabortty, J. A. Yang, Y. M. Tan, N. Mishra and Y. Chan, *Angew. Chem.*, 2010, **49**, 2888.
9 D. Nagao, C. M. van Kats, K. Hayasaka, M. Sugimoto, M. Konno, A. Imhof and A. van Blaaderen, *Langmuir*, 2010, **26**, 5208.
10 D. Nagao, M. Sugimoto, A. Okada, H. Ishii, M. Konno, A. Imhof and A. van Blaaderen, *Langmuir*, 2012, **28**, 6546.
11 K. Yoon, D. Lee, J. W. Kim, J. Kim and D. A. Weitz, *Chem. Commun.*, 2012, **48**, 9056.
12 J. D. Forster, J. G. Park, M. Mittal, H. Noh, C. F. Schreck, C. S. O'Hern, H. Cao, E. M. Furst and E. R. Dufresne, *ACS Nano*, 2011, **5**, 6695.
13 F. Ma, S. Wang, L. Smith and N. Wu, *Adv. Funct. Mater.*, 2012, **22**, 4334.
14 I. D. Hosein and C. M. Liddell, *Langmuir*, 2007, **23**, 10479.
15 K. Milinkovic, M. Dennison and M. Dijkstra, *Phys. Rev. E: Stat., Nonlinear, Soft Matter Phys.*, 2013, **87**, 032128.
16 G. Munaò, D. Costa and C. Caccamo, *Chem. Phys. Lett.*, 2009, **470**, 240.
17 G. Munaò, D. Costa and C. Caccamo, *J. Chem. Phys.*, 2009, **130**, 144504.
18 M. Marechal and M. Dijkstra, *Phys. Rev. E: Stat., Nonlinear, Soft Matter Phys.*, 2008, **77**, 061405.
19 R. Ni and M. Dijkstra, *J. Chem. Phys.*, 2011, **134**, 034501.
20 M. Marechal, H. H. Goetzke, A. Härtel and H. Löwen, *J. Chem. Phys.*, 2011, **135**, 234510.
21 G. A. Chapela and J. Alejandre, *J. Chem. Phys.*, 2010, **132**, 104704.
22 G. A. Chapela, F. de Rio and J. Alejandre, *J. Chem. Phys.*, 2011, **134**, 224105.
23 G. A. Chapela and J. Alejandre, *J. Chem. Phys.*, 2011, **135**, 084126.
24 G. Munaò, D. Costa, A. Giacometti, C. Caccamo and F. Sciortino, *Phys. Chem. Chem. Phys.*, 2013, **15**, 20590.
25 M. A. Miller, R. Blaak, C. N. Lumb and J.-P. Hansen, *J. Chem. Phys.*, 2009, **130**, 114507.
26 P. Ilg and E. Del Gado, *Soft Matter*, 2011, **7**, 163.
27 S. H. Chong, A. J. Moreno, F. Sciortino and W. Kob, *Phys. Rev. Lett.*, 2005, **94**, 215701.
28 G. Munaò, Z. Preisler, T. Vissers, F. Smallenburg and F. Sciortino, *Soft Matter*, 2013, **9**, 2652.
29 M. Tarzia and A. Coniglio, *Phys. Rev. Lett.*, 2006, **96**, 075702.
30 A. de Candia, E. D. Gado, A. Fierro, N. Sator, M. Tarzia and A. Coniglio, *Phys. Rev. E: Stat., Nonlinear, Soft Matter Phys.*, 2006, **74**, 010403.
31 M. Tarzia and A. Coniglio, *Phys. Rev. E: Stat., Nonlinear, Soft Matter Phys.*, 2007, **75**, 011410.
32 W. L. Miller and A. Cacciuto, *Phys. Rev. E: Stat., Nonlinear, Soft Matter Phys.*, 2009, **80**, 021404.
33 A. Saric, B. Bozorgui and A. Cacciuto, *J. Phys. Chem. B*, 2011, **115**, 7182.
34 Y. Sheng, X. Yang, N. Yan and Y. Zhu, *Soft Matter*, 2013, **9**, 6254.
35 T. Vissers, Z. Preisler, F. Smallenburg, M. Dijkstra and F. Sciortino, *J. Chem. Phys.*, 2013, **138**, 164505.
36 F. Tu, B. J. Park and D. Lee, *Langmuir*, 2013, **29**, 12679.
37 B. J. Park and D. Lee, *ACS Nano*, 2012, **6**, 782.
38 A. M. Jackson, J. W. Myerson and F. Stellacci, *Nat. Mater.*, 2004, **3**, 330–336.
39 K.-H. Roh, D. C. Martin and J. Lahann, *Nat. Mater.*, 2005, **4**, 759–763.
40 B. Wang, B. Li, B. Zhao and C. Y. Li, *J. Am. Chem. Soc.*, 2008, **130**, 11594–11595.
41 L. Hong, A. Cacciuto, E. Luijten and S. Granick, *Langmuir*, 2008, **24**, 621–625.
42 A. Walther and H. Müller, *Soft Matter*, 2008, **4**, 663.
43 C.-H. Chen, R. K. Shah, A. R. Abate and D. A. Weitz, *Langmuir*, 2009, **25**, 4320–4323.
44 B. S. Jiang, Q. Chen, M. Tripathy, E. Luijten, K. Schweizer and S. Granick, *Adv. Mater.*, 2010, **22**, 1060.
45 Q. Chen, J. K. Whitmer, S. Jiang, S. C. Bae, E. Luijten and S. Granick, *Science*, 2011, **331**, 199.
46 R. Fantoni, A. Giacometti, F. Sciortino and G. Pastore, *Soft Matter*, 2011, **7**, 2419.
47 F. Sciortino, A. Giacometti and G. Pastore, *Phys. Rev. Lett.*, 2009, **103**, 237801.

48 F. Sciortino, A. Giacometti and G. Pastore, *Phys. Chem. Chem. Phys.*, 2010, **12**, 11869.
49 P. Virnau and M. Müller, *J. Chem. Phys.*, 2004, **120**, 10925–10930.
50 A. M. Ferrenberg and R. H. Swendsen, *Phys. Rev. Lett.*, 1989, **63**, 1195–1198.
51 B. J. Schulz, K. Binder, M. Müller and D. P. Landau, *Phys. Rev. E: Stat., Nonlinear, Soft Matter Phys.*, 2003, **67**, 067102.
52 D. Frenkel and B. Smit, *Understanding Molecular Simulations*, Academic, New York, 1996.
53 M. Floriano, E. Caponetti and A. Z. Panagiotopoulos, *Langmuir*, 1999, **15**, 3143.
54 F. Sciortino, A. Giacometti and G. Pastore, *Phys. Chem. Chem. Phys.*, 2010, **12**, 11869.
55 U. Gasser, A. Schofield and D. A. Weitz, *J. Phys.: Condens. Matter*, 2003, **15**, S375.
56 F. Cardinaux, A. Stradner, P. Schurtenberger, F. Sciortino and E. Zaccarelli, *Europhys. Lett.*, 2007, **77**, 48004.
57 J. M. Bomont, J. L. Bretonnet and D. Costa, *J. Chem. Phys.*, 2010, **132**, 084506.
58 J.-M. Bomont, J.-L. Bretonnet, D. Costa and J.-P. Hansen, *J. Chem. Phys.*, 2012, **137**, 011101.
59 M. Dennison, K. Milinkovic and M. Dijkstra, *J. Chem. Phys.*, 2012, **137**, 044507.